The Meteoritical Society

Meteoritics & Planetary Science 42, Nr 2, 235–253 (2007)
Abstract available online at http://meteoritics.org

Spectroscopy of synthetic Mg-Fe pyroxenes I: Spin-allowed and spin-forbidden crystal field bands in the visible and near-infrared

Rachel L. KLIMA[1*], Carlé M. PIETERS[1], and M. Darby DYAR[2]

[1]Department of Geological Sciences, Brown University, Providence, Rhode Island 02912, USA
[2]Department of Astronomy, Mount Holyoke College, South Hadley, Massachusetts 01075, USA
[*]Corresponding author. E-mail: Rachel_Klima@brown.edu

(Received 30 August 2006; revision accepted 05 December 2006)

Abstract–Understanding the fundamental crystal chemical controls on visible and near-infrared reflectance spectra of pyroxenes is critical to quantitatively assessing the mineral chemistry of pyroxenes viewed by remote sensing. This study focuses on the analysis of spectroscopic measurements of a comprehensive set of synthetic Mg-Fe pyroxenes from the visible through the near-infrared (0.3–2.6 μm) to address the constraints of crystal structure and Fe^{2+} content on spin-forbidden and spin-allowed crystal field absorptions in Ca-free orthopyroxenes. The chemistry and oxidation state of the synthetic pyroxenes are characterized. Coordinated Mössbauer spectroscopy is used to determine site occupancy of Fe^{2+} in the M1 and M2 crystallographic sites. Properties of visible and near-infrared absorption bands of the synthetic pyroxenes are quantified using the modified Gaussian model. The 1 and 2 μm spin-allowed crystal field absorption bands move regularly with increasing iron content, defining a much tighter trend than observed previously. A spin-allowed crystal field absorption band at 1.2 μm is explicitly verified, even at low total iron contents, indicating that some portion of Fe^{2+} resides in the M1 site. The 1.2 μm band intensifies and shifts to longer wavelengths with increasing iron content. At visible wavelengths, spin-forbidden crystal field absorptions are observed in all iron-bearing samples. The most prominent absorption near 506 nm, attributed to iron in the M2 site, shifts to slightly longer wavelengths with iron content. The purity and extent of this pyroxene series allows visible wavelength absorption bands to be directly assigned to specific transitions of Fe^{2+} in the M1 and M2 sites.

INTRODUCTION

Pyroxene is one of the most common minerals in both evolved and undifferentiated solid bodies of the solar system. Prominent absorption features in the visible and near-infrared easily distinguish pyroxene from other minerals and are dependent on composition (Adams 1974; Burns 1993). This makes pyroxene a very useful mineral for remote geochemical analysis. Near-infrared studies of natural pyroxenes have revealed that changes in the positions of absorption bands are directly related to the primary octahedral pyroxene cations (Ca, Mg, and Fe), although substitutions of minor cations such as Ti^{4+}, Cr^{3+}, Fe^{3+}, and Al^{3+} also affect absorption features and can lead to misclassification of pyroxene compositions (Adams 1974; Sunshine et al. 1990; Cloutis and Gaffey 1991b; Sunshine and Pieters 1993; Hamilton 2000; Cloutis 2002). The challenge for remote analyses has thus been to reduce the level of ambiguity in order to allow a quantitative assessment of mineral chemistry. This study focuses on a Ca-free endmember suite of synthetic pyroxenes in order to address the fundamental constraints of crystal structure and Mg-Fe^{2+} content on visible and near-infrared (0.3–2.6 μm) reflectance spectra.

BACKGROUND

Visible and Near-Infrared Spectroscopy

The use of pyroxene spectroscopy for compositional analysis has been the focus of much research since the 1970s (e.g., Burns et al. 1972; Adams 1974; Hazen et al. 1978; Cloutis and Gaffey 1991a). Most of this research has centered on the behavior of the prominent 1 and 2 μm spin-allowed crystal field absorptions that are readily observable on the Moon, Mars, and asteroids (e.g., Gaffey et al. 1993; Pieters 1993; Pieters and McFadden 1994; Bibring et al. 2005; Mustard et al. 2005). In addition to the spin-allowed absorption bands, there are a number of spin-forbidden crystal

field absorptions in the visible spectra of Fe-bearing pyroxenes. Although these visible features are orders of magnitude weaker than those in the near-infrared, they have been detected on Vesta and other smaller asteroids and are being investigated as compositional indicators (Golubeva and Shestopalov 1997, 2006; Cochran and Vilas 1998; Vilas et al. 2000). With the exception of early transmission spectroscopy of lunar and terrestrial pyroxenes (Burns et al. 1967, 1972, 1973; Hazen et al. 1978; Goldman and Rossman 1979), there has been little systematic characterization of visible wavelength pyroxene features as a function of chemistry, especially on simple, synthetic compositions for which peak assignments are tractable.

As single-chain silicates, pyroxenes can accommodate cations in tetrahedral or octahedral coordination. Si and sometimes Al occupy the tetrahedral sites. Ca-free pyroxenes most commonly occur with orthorhombic symmetry. Although it is possible to synthesize Ca-free pyroxenes with a monoclinic structure, the current study focuses on orthopyroxenes. The M1 and M2 octahedral sites in orthopyroxenes contain primarily Fe^{2+} and Mg, but may also contain Ti^{4+}, Cr^{3+}, Fe^{3+}, Al, and small amounts of Ca and Na. The M1 site is coordinated to six nonbridging oxygens, resulting in higher symmetry than that of the more distorted M2 site, which is coordinated to four nonbridging and two bridging oxygens. The M1 site has a mean metal-oxygen distance ranging from 2.08 Å (pure Mg) to 2.14 Å (pure Fe^{2+}), while the M2 site is larger with a mean metal-oxygen distance of 2.15–2.23 Å. The size, symmetry, and cation occupancy of the M1 and M2 sites directly affect the positions and strengths of absorption features caused by electronic transitions in the visible and near-infrared (Burns 1993).

Absorption features at visible and near-infrared wavelengths are attributed to four processes (e.g., Burns 1993): 1) oxygen-metal charge transfers, 2) intervalence charge transfers, 3) spin-allowed crystal field transitions, and 4) spin-forbidden crystal field transitions. Oxygen-metal charge transfers are generally centered at energies within the ultraviolet, but have intensities several orders of magnitude stronger than spin-allowed crystal field transitions. The edges of these absorption bands thus extend into the visible, and may overlap absorptions caused by other electronic processes. Intervalence charge transfers occur when more than one valence state or species of a transition metal cation (often Fe and/or Ti) is present in a mineral. Intervalence charge transfers are also stronger (~1–2 orders of magnitude) than typical crystal field transitions, and are primarily centered at visible wavelengths.

Spin-allowed and spin-forbidden crystal field transitions take place when transition metal cations reside in a ligand field. The surrounding ligands produce an asymmetric electrostatic field, splitting the energy levels of *d*-orbital electrons of the cations. An incident photon may be absorbed at certain wavelengths, exciting an electron from a lower to a higher energy state (Burns 1993). If the electronic transition is spin-allowed, it produces a prominent absorption feature such as the familiar 1 and 2 μm Fe^{2+} pyroxene bands (e.g., Adams 1974; Cloutis and Gaffey 1991a). The relative intensities of such absorptions increase with the asymmetry of the octahedral site (Burns 1993). Thus, Fe^{2+} in the M2 site in pyroxene results in the very strong 1 and 2 μm absorptions, while the more symmetric M1 site produces weaker absorptions. Spin-allowed crystal field transitions due to Fe^{2+} are centered in the near infrared, but those caused by other transition metals (Cr, Ti, etc.) may occur at both visible and near-infrared wavelengths (Burns 1993).

Spin-forbidden bands are observed as a series of sharp absorptions that are ~1–2 orders of magnitude weaker than spin-allowed crystal field transitions, and several are centered at visible wavelengths. Assignment of spin-forbidden bands is extremely complicated in a natural pyroxene because many weak features may be present, even in a system where the only transition metal is Fe^{2+}. Table 1 summarizes some of the spin-forbidden features that have been observed by previous authors, as well as tentative band assignments that have been proposed based on theoretical and experimental considerations (Burns et al. 1972, 1973; Hazen et al. 1978; Goldman and Rossman 1979). If Fe^{3+}, Ti, and/or Cr are also present, these features may be superimposed by intervalence charge transfers and/or spin-allowed crystal field bands, and are therefore not always discernible.

Previous spectroscopic studies of terrestrial and lunar pyroxenes have provided a foundation for understanding the behavior of a pyroxene spectrum as a function of chemical composition (e.g., Burns et al. 1972; Adams 1974; Hazen et al. 1978; Cloutis and Gaffey 1991a). Although great care has been taken to document natural pyroxene chemistries in these studies, the numbers of cations and valences makes assignment of bands, particularly in the visible region, extremely difficult. The number of unknown variables can be drastically reduced by using well-characterized synthetic pyroxenes that are restricted to contain only Mg and Fe^{2+} in the octahedral sites, substantially reducing the uncertainty of band assignment.

Mössbauer Spectroscopy

As with visible to near-infrared spectra, features in Mössbauer spectra are controlled by the crystal environment. While visible and near-infrared spectra measure absorptions due to electronic transitions, Mössbauer spectra measure absorptions caused by nuclear energy transitions. Mössbauer spectra are sensitive to the valence state of iron, the symmetry of the cation site, the surrounding anion environment, and the presence or absence of magnetic ordering A detailed review of Mössbauer spectroscopy can be found in Dyar et al. (2006). Mössbauer spectra in paramagnetic minerals such as pyroxene can be described in terms of an isomer shift and

Table 1. Previous positions and assignments of visible wavelength pyroxenes features based on transmission measurements.

Mineral	References[a]	Wavelength (nm)										
Lunar CPX	1	402	425	–	465	–	–	505	552	585	–	655
10047	–	Fe^{2+}	Fe^{2+}	–	Ti^{3+}	–	–	Fe^{2+}	Fe^{2+}	Fe^{2+}	–	Ti^{3+}
Terrestrial	1	–	–	450	–	–	–	505	555	–	–	660
Titan-augite	–	–	–	Ti^{3+}	–	–	–	Fe^{2+}	Fe^{2+}	–	–	Ti^{3+}
Lunar augite	3	–	435	–	475	–	–	507	550	–	–	–
73261-4	–	–	–	–	–	–	–	–	–	–	–	–
Synthetic $FeSiO^3$	3	–	437	–	–	480	–	508.5	550	–	–	–
Lunar pigeonite	3	–	425	–	470	–	–	505	550	–	–	–
12033-4	–	–	–	–	–	–	–	–	–	–	–	–
Lunar zoned pyx	2	400	430	450	470	–	–	503/8	550	–	600	–
15058: core (pig)	–	–	Fe^{2+}	Cr^{3+}	Ti^{3+}	–	–	Fe^{2+}M1/M2	Fe^{2+}	–	Cr^{3+}	–
Lunar zoned pyx	2	–	430	450	470	–	–	505	550	–	600	650
15058: mid (aug)	–	–	Fe^{2+}	–	Ti^{3+}	–	–	Fe^{2+}	Fe^{2+}	–	Cr^{3+}	Ti^{3+}
Lunar zoned pyx	2	400	430	–	470	–	–	505	550	–	–	650
15058: core (Fe-aug)	–	–	Fe^{2+}	–	Ti^{3+}	–	–	Fe^{2+}	Fe^{2+}	–	–	Ti^{3+}
Terrestrial bronzite	4	–	426	446	468	481	489	506/507.6	548	–	–	–
Gore Mountain	–	–	Fe^{2+}M2	Fe^{2+}M2	Fe^{2+}M1	Fe^{2+}M2	Fe^{2+}M1	Fe^{2+}M2/M1	Fe^{2+}M2	–	–	–

[a] 1 = Burns et al. (1972); 2 = Burns et al. (1973); 3 = Hazen et al. (1978); 4 = Goldman and Rossman (1979).

quadrupole splitting. An isomer shift is caused by the difference in the s-orbital electron density between the nuclei of the ^{57}Co source and the sample. In Fe^{2+} bearing pyroxenes, this difference, measured with respect to the isomer shift of α-Fe foil, generally ranges from 1.13 to 1.18 mm/s. The quadrupole splitting, which can be measured in a Mössbauer spectrum by the distance between the two peaks in a doublet, is a result of the splitting of the nuclear quadrupole moment by the local ligand field.

Early Mössbauer studies of orthopyroxenes found that when a spectrum was modeled with only a single doublet, the fit was poor and unlikely to accurately represent the isomer shift and quadrupole splitting parameters. If two doublets are instead considered, the error in the modeled fit drastically decreases (Evans et al. 1967). This is attributed to the differing environments around Fe^{2+} in the M1 and M2 sites, each with slightly different Mössbauer parameters. The more absorbing, inner doublet (smaller quadrupole splitting), has been unambiguously assigned to the M2 site by numerous authors, as Fe^{2+} is known to prefer the M2 site in orthopyroxenes (e.g., Bancroft et al. 1967; Evans et al. 1967; Saxena and Ghose 1971). Typical values of quadrupole splitting for the M1 site in pyroxenes range from 1.9–2.1 mm/s and for the M2 site range from 2.49–2.59 mm/s (Evans et al. 1967; Dowty and Lindsley 1973; Johnston and Knedler 1979; Lin et al. 1993; Van Alboom et al. 1993). When Fe^{3+} is also present in a pyroxene, a third and sometimes fourth doublet appears, depending on whether the ferric iron is in tetrahedral or octahedral coordination or both. These doublets are readily distinguishable in Mössbauer spectra of pyroxenes, as they have a much smaller isomer shift and quadrupole splitting than ferrous iron in the M1 or M2 site. Mössbauer spectroscopy can thus be used to evaluate the valence state of iron and to estimate the proportion of Fe^{2+} in the M1 and M2 sites, providing further constraints when analyzing visible and near-infrared spectra.

EXPERIMENTAL METHODS

Chemical Characterization of Pyroxenes

The pyroxenes used in this study were synthesized by Don Lindsley and colleagues between 1972 and 2006 using the procedures detailed in Turnock et al. (1973). All samples were prepared from reagent-grade chemicals and the oxygen fugacity was buffered at the iron-wüstite curve. The pressures, temperatures, and run times for each of the pyroxenes used in this study are summarized in Table 2. For each composition, a series of experimental runs was completed. The position in the sequence is indicated by a letter in the "Run" column of Table 2, with "A" being the first batch run at that composition, and subsequent letters representing batches that in some cases contained pre-reacted, reground material or seed grains from previous runs. Samples 002 and 024 were synthesized with seed grains from 027 and 020, respectively. Specific methods varied by composition, and were chosen to prevent nucleation of pyroxenoids and produce a single, homogeneous pyroxene. Pyroxene

Table 2. Synthesis conditions for the pyroxene samples.

Sample	Mg	Fe	Run	T (°C)	P (Kbar)	Time (h)
001	100	0	A	950	20	10
064	90	10	G	950–990	20	12.2
065	97.5	2.5	A	965–1005	20	6
002	80	20	E	970–980	20	10
027	80	20	C	950	20	5
022	75	25	A	960–1000	20	2
003	75	25	F	970–980	20	5
026	70	30	B	950	20	10
004	50	50	F	980	20	10
025	35	65	A	970–980	20	10
023	30	70	A	930–980	20	9
028	25	75	C	900	20	5.5
024	17	83	C	970–980	20	10
020	17	83	A	920	20	12.5
021	8	92	A	960–1000	20	2.8
061	0	100	PP1	940–980	20	14

compositions were validated by Lindsley and colleagues using X-ray diffraction. Any samples that were reported to be clinopyroxene were excluded from this study.

The synthesis procedures outlined above produce pyroxenes that are fine powders, with individual grains approximately 15–25 μm in diameter. Powders were photographed under a binocular microscope to document the range in grain sizes present. Many of the powders formed clumps of grains, which were crushed manually and sieved to <45 μm and >45 μm grain size fractions for further analysis. The <45 μm size fraction was used for Vis/NIR and Mössbauer spectroscopy, and, when available, the >45 μm size fraction was used to prepare grain mounts for electron microprobe analysis. Between 12–41 mg of each pyroxene was mixed with sugar, ground under acetone, and mounted for collection of Mössbauer spectra.

Though the starting composition of all pyroxenes is known, purity of samples was verified using the CAMECA SX-100 electron microprobe at Brown University. Electron backscatter was used to identify samples with unreacted starting oxides or excess mineral phases. Sixteen pyroxenes, with compositions ranging from En_{100}–En_0, were chosen for detailed characterization on the basis of their homogeneous chemical composition. Any samples with accessory iron-bearing phases, such as olivine or iron metal, were excluded from this study. Throughout the remainder of this manuscript, "total iron" will refer to number of moles (n) of Fe^{2+} relative to the total number of moles of M1 and M2 cations, or $n_{Fe^{2+}} / (n_{Fe^{2+}} + n_{Mg}) \times 100$, and Mg number (Mg#) will refer to $n_{Mg} / (n_{Fe^{2+}} + n_{Mg}) \times 100$.

Visible and Near-Infrared Spectroscopy and Modeling

Visible and near-infrared spectra were collected using the Bidirectional Reflectance Spectrometer (BDR) at the NASA/Keck Reflectance Experiment Lab (RELAB) at Brown University. Spectra of the <45 μm grain size fraction were measured relative to a halon reference standard at 5 nm intervals over the wavelength range of 0.3–2.6 μm and corrected for the small features of halon. An incidence angle of 30° and an emission angle of 0° were selected for bidirectional measurements. High-resolution (0.5 nm interval) spectra were also collected in the visible between 0.4–0.6 μm. Diffuse reflectance spectra for the wavelength range of 1.7–50 μm were additionally collected and will be discussed in a subsequent paper.

Spin-allowed and spin-forbidden crystal field bands in the visible and near-infrared were modeled using the modified Gaussian model (MGM). The MGM deconvolves a spectrum into a continuum and a series of modified Gaussian curves that can be attributed to specific absorptions (Sunshine et al. 1990; Sunshine et al. 1999). The visible portion of the spectrum is a complex superposition of weak spin-forbidden absorptions on very strong metal-oxygen charge transfer absorptions. The following steps were developed to constrain the MGM fits to accommodate both the spin allowed and spin forbidden bands:

1. For this group of samples, a straight line in wavenumber (energy, cm^{-1}) space was fit to the peak reflectance on either side of the 2 μm absorption band. The slope of the continuum in the MGM input file was constrained to be parallel to this line, but the offset was allowed to move freely.
2. A fit of the 5 nm resolution visible to near-infrared data was performed using the above-mentioned continuum constraints, 2–3 broad bands in the visible (representing Fe^{2+}-O charge transfers), and 3–4 bands in the near-infrared (representing spin-allowed crystal field bands). Initial starting parameters for these bands were chosen visually for pyroxene 002 (Mg80). The starting continuum, 5 nm resolution, and 0.5 nm resolution parameters for this sample are given in Table 3. The

resulting band parameters were used as starting parameters for fitting the pyroxenes of the most similar iron content. Similarly, the resulting band parameters from the next run were used to begin the subsequent pyroxene in the series. This process was repeated for the remainder of the pyroxenes.

3. The continuum and band positions derived for the lower-resolution 5 nm data were then used for the input file for the high-resolution (0.5 nm) visible data. An additional 4–6 narrow, weak bands were added to account for the spin-forbidden absorption features. These bands were fit with the continuum slope held constant.
4. Adding the derived spin-forbidden band parameters to the lower-resolution near-infrared spectra, a final fit was performed using 11–12 total bands. Again, the only restricted parameter was the slope of the continuum.

Mössbauer Spectroscopy

Mössbauer spectra were collected at Mount Holyoke College using a WEB Co. model W100 spectrometer with a 45 mCi ^{57}Co in Rh source. Samples other than En_{100} (sample 001) were run at room temperature for roughly 6 hours, until a minimum of 3,000,000 counts was returned. En_{100}, which contains only trace amounts of iron present as contaminants in the reagents, was run for five days to obtain a clean spectrum. Spectra were calibrated against an α-Fe foil of 6 μm thickness and 99% purity.

Mössbauer spectra are fit by modeling the parameter distribution functions of overlapping doublets. Pyroxene spectra were fit using software based upon the work of Wivel and Mørup (1981), which models the distribution function using a least squares regression. An implementation of this software, Mex_FieldDD, as developed at the University of Ghent by E. DeGrave and T. Van Alboom, was used to process our data. A starting isomer shift and line width at half maximum for each doublet is input into the model, along with a range of quadrupole splitting values. Although isomer shifts and line widths may be held fixed, starting parameters were adjusted until the model produced an acceptable fit with all variables unconstrained. Data were then corrected for thickness and the effects of differential recoil-free fraction (see Dyar et al. 2007 for details). Errors on isomer shift and quadrupole splitting are ±0.02 mm/s, and errors on peak areas are ±<1% absolute.

RESULTS

Electron Microprobe Analysis

A total of 22 Mg-Fe synthetic pyroxenes were acquired from Don Lindsley and Allan Turnock. Three pyroxenes were excluded from this study due to the presence of excess iron-bearing phases within the mineral grains (i.e., fayalite or iron metal blebs), and three others contained insufficient material for full analysis. The remaining pyroxenes range in composition from En_{100}– En_0, with 13 unique Mg-Fe ratios. Results of electron microprobe analyses for this series are presented in Table 4. Additional pyroxenes were available at compositions of En_{80}, En_{75}, and En_{17}. The latest batches were selected for each of the pyroxenes at these compositions, on the basis that earlier batches were either used to seed the later runs or run at slightly lower temperatures for shorter times. The sample number for each of the earlier batches (duplicates) is shown in parentheses in Table 4. These duplicate pyroxenes were of the same composition as the later runs within the standard deviation.

Table 3. Starting MGM parameters for pyroxene 002 (Mg80).

Band	Center	FWHM	Intensity
5 nm resolution, 0.3–2.6 μm			
1	310	95	−2.10
2	440	130	−0.25
3	550	180	−0.10
4	910	200	−1.75
5	1150	260	−0.60
6	1860	600	−1.00
7	2500	500	−0.11
0.5 nm resolution, 400–600 nm			
1	427	4	−0.04
2	467	6	−0.01
3	505	6	−0.09
4	549	2	−0.03
Continuum			
Slope	−1.3E-5		
Offset	8.9E-1		

Mössbauer Spectroscopy

Mössbauer spectra for the main pyroxene series are presented in Figs. 1a and 2. The Mössbauer parameters and normalized χ^2 of the model fits are given in Table 5. All spectra but that of En_{100} were fit by two doublets (Fig. 2), which are attributed to Fe^{2+} in the M1 and M2 sites (e.g., Bancroft et al. 1967; Evans et al. 1967; Saxena and Ghose 1971). The M2 doublet, which has a smaller quadrupole splitting, is shown in dark gray in Fig. 2 and dominates the spectrum of the low iron (≤Fs_{30}) pyroxenes. At higher iron contents, the M1 doublet (light gray) grows until the percent area for the M1 site is almost equal to that of the M2 site. As is well known from the literature, Fe^{2+} is only completely disordered in the endmember ferrosilite; in all other cases, Fe^{2+} is ordered to some extent into the M2 sites. This conclusion is in keeping with previous studies of natural samples using Mössbauer (e.g., Bancroft et al. 1967; Virgo and Hafner 1970; Saxena and Ghose 1971; Besancon 1981; Anovitz et al. 1988), X-ray diffraction (e.g., Burnham et al.

Table 4. Chemical compositions of synthetic pyroxenes.

Sample	001	064	065	002 (027)	003 (022)	026	004	025	023	028	024 (020)	021	061
Mg#	100	97.5	90	80	75	70	50	35	30	25	17	8	0
SiO_2	59.86	59.61	58.19	56.50	55.73	55.29	51.72	49.73	49.03	48.37	47.47	46.27	44.81
Al_2O_3	0.06	0.01	0.02	0.03	n.d.	0.01	0.02	0.10	0.01	0.06	0.01	n.d.	n.d.
FeO	0.06	1.83	6.69	13.60	15.65	18.23	31.07	38.86	40.66	42.89	46.61	50.34	54.35
MnO	n.d.	0.01	n.d.	n.d.	n.d.	0.03	n.d.	n.d.	0.02	0.04	n.d.	n.d.	0.02
MgO	39.75	38.85	35.50	29.94	28.68	26.61	17.16	11.60	9.88	7.84	5.42	2.47	n.d.
CaO	0.03	n.d.	0.01	0.02	0.03	0.03	0.02	n.d.	0.01	0.03	0.02	n.d.	0.01
Total	99.8	100.3	100.4	100.1	100.1	100.2	100.0	100.3	99.6	99.2	99.5	99.1	99.2
Percent Fe^{3+}	66	0	0	0	0	0	0	0	0	0	0	0	0
Si	2.005	2.002	1.996	2.005	1.998	2.004	2.001	1.997	2.003	2.009	2.005	2.007	1.990
Al	0.002	n.d.	0.001	0.001	n.d.	n.d.	0.001	0.005	n.d.	0.003	n.d.	n.d.	0.001
Fe^{2+}	0.001	0.051	0.192	0.404	0.469	0.553	1.005	1.305	1.389	1.490	1.647	1.826	2.018
Fe^{3+}	0.001	n.d.	n.d.	n.d.	n.d.	n.d.	n.d.	n.d.	n.d.	n.d.	n.d.	n.d.	n.d.
Mn	n.d.	n.d.	n.d.	n.d.	n.d.	n.d.	n.d.	n.d.	n.d.	0.001	n.d.	n.d.	0.001
Mg	1.984	1.944	1.815	1.584	1.533	1.437	0.990	0.694	0.602	0.485	0.341	0.160	n.d.
Ca	0.001	n.d.	n.d.	0.001	0.001	0.001	0.001	n.d.	n.d.	0.001	0.001	n.d.	n.d.

Percent Fe^{3+} is as determined by Mössbauer spectroscopy. Na_2O was not detected in any sample. TiO_2 was detected at 0.01 wt% only in sample 023; Cr_2O_3 was observed at 0.01 wt% only in samples 004, 023, and 064.

Table 5. Mössbauer parameters for synthetic Mg-Fe pyroxenes.

Sample number	Mg#	Total Fe	Fe^{2+} in M2				Fe^{2+} in M1				χ^2	$n_{Fe^{2+}(M1)}/n_{Fe^{2+}(M2)}$[a]
			IS	QS	Γ	Area	IS	QS	Γ	Area		
001	100	0	1.11	2.07	0.25	17	1.17	2.65	0.25	13	8.6	n.d.
064	97.5	2.5	1.14	2.12	0.26	86	1.17	2.55	0.26	14	1.6	0.163
065	90	10	1.14	2.09	0.26	84	1.16	2.45	0.26	16	1.4	0.176
002	80	20	1.15	2.10	0.30	83	1.17	2.47	0.30	18	1.9	0.198
027	80	20	1.15	2.11	0.30	84	1.17	2.50	0.30	16	1.7	0.183
003	75	25	1.15	2.10	0.31	81	1.17	2.48	0.31	19	2.0	0.220
022	75	25	1.15	2.10	0.27	82	1.17	2.50	0.27	18	2.1	0.202
026	70	30	1.15	2.09	0.32	81	1.17	2.49	0.32	19	2.7	0.217
004	50	50	1.15	2.05	0.31	74	1.17	2.49	0.31	26	4.4	0.323
025	35	65	1.14	2.03	0.25	67	1.18	2.49	0.25	33	8.1	0.442
023	30	70	1.14	2.02	0.28	65	1.18	2.50	0.28	35	3.6	0.459
028	25	75	1.14	2.00	0.26	62	1.18	2.49	0.26	38	1.3	0.504
024	17	83	1.14	1.98	0.27	57	1.19	2.50	0.27	43	2.8	0.569
020	17	83	1.14	1.99	0.25	57	1.18	2.50	0.25	43	3.5	0.703
021	8	92	1.14	1.97	0.27	52	1.19	2.51	0.27	48	4.7	0.708
061	0	100	1.13	1.92	0.31	48	1.18	2.51	0.31	52	7.6	0.851

[a]Site occupancy calculated in Dyar et al. (2007).

IS = isomer shift; QS = quadrupole splitting; Γ = line width at half-maximum.

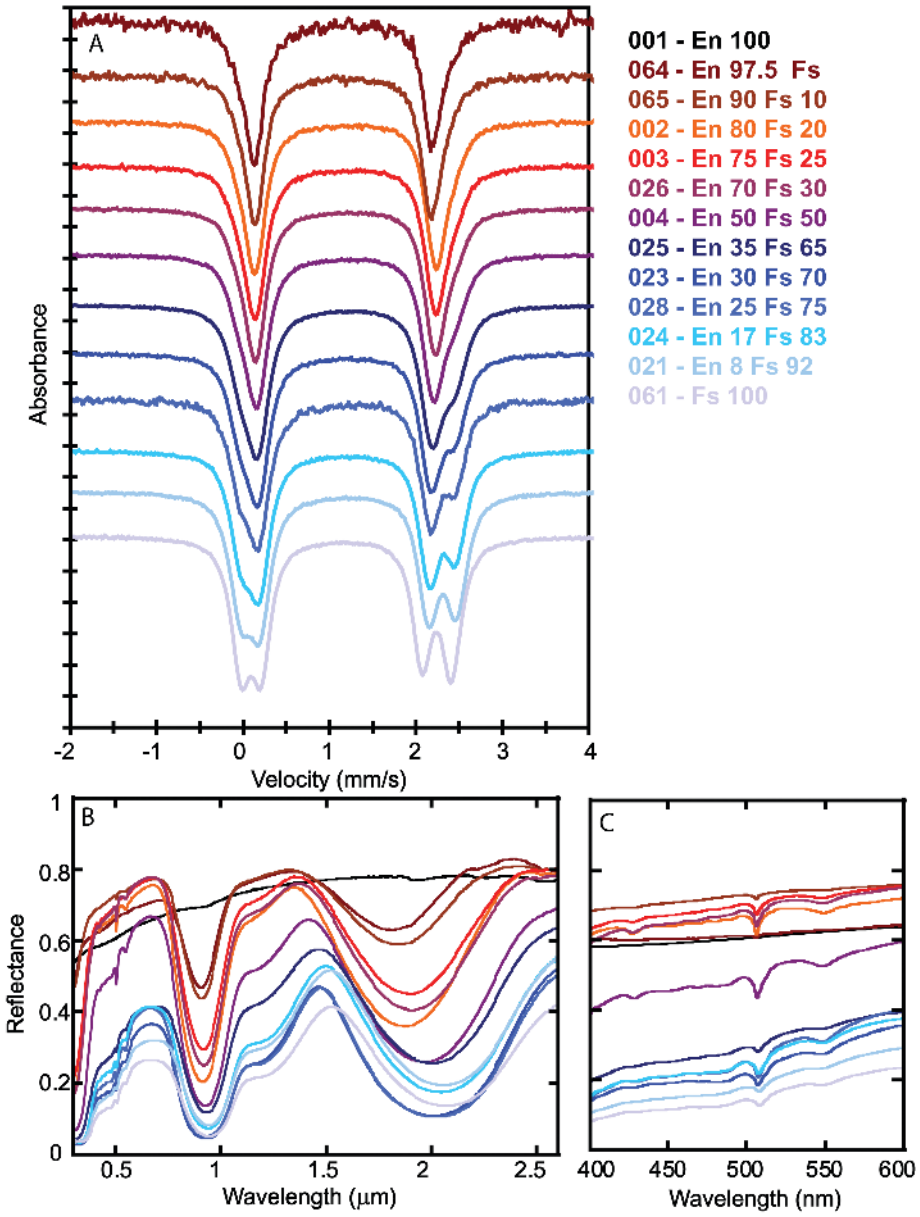

Fig. 1. a) Mössbauer spectra of synthetic pyroxene series. The iron content of pyroxenes increases downward, with lower-iron pyroxenes colored red and higher-iron pyroxenes colored blue. b) Near-infrared spectra of synthetic pyroxene series. With increasing iron content, each of the spin-allowed crystal field absorptions shift to longer wavelengths. c) High-resolution (0.5 nm) visible spectra of the synthetic pyroxenes. The color coding of each composition is the same for each of the three panels.

1971; Ghose and Wan 1973; Ghose et al. 1975) and FTIR spectra (Goldman and Rossman 1979).

The areas of the doublets that comprise a Mössbauer spectrum, once corrected for thickness, differential recoil-free fraction, and saturation (Dyar et al. 2007), are proportional to the relative number of atoms of the species represented by the doublet. The M1 and M2 site occupancy and the oxidation state of iron in a pyroxene can be calculated using the ratios of the corrected areas of the doublets comprising the Mössbauer spectrum (e.g., Preston et al. 1962; Bancroft et al. 1967; Bancroft 1969). Site occupancies for Fe^{2+} in the M1 and M2 sites (n_{M1}/n_{M2}) of each of the pyroxenes as calculated in Dyar et al. (2007) are included in Table 5, and the relative proportions of Fe^{2+} in the M1 and M2 sites relative to total iron in each pyroxene are illustrated in Fig. 3. As expected, the ratio of iron in the M1/M2 sites increases with increasing total iron content. However, note that even at the lowest total iron contents, some iron still resides in the M1 site.

None of the synthetic pyroxenes shows significant Fe^{3+}. With the exception of En_{100}, <1% of the total Fe in each of the samples is Fe^{3+}. In En_{100}, which contains only 0.06% total iron, 66% of the Fe is present as Fe^{3+}, or 0.001 cations per

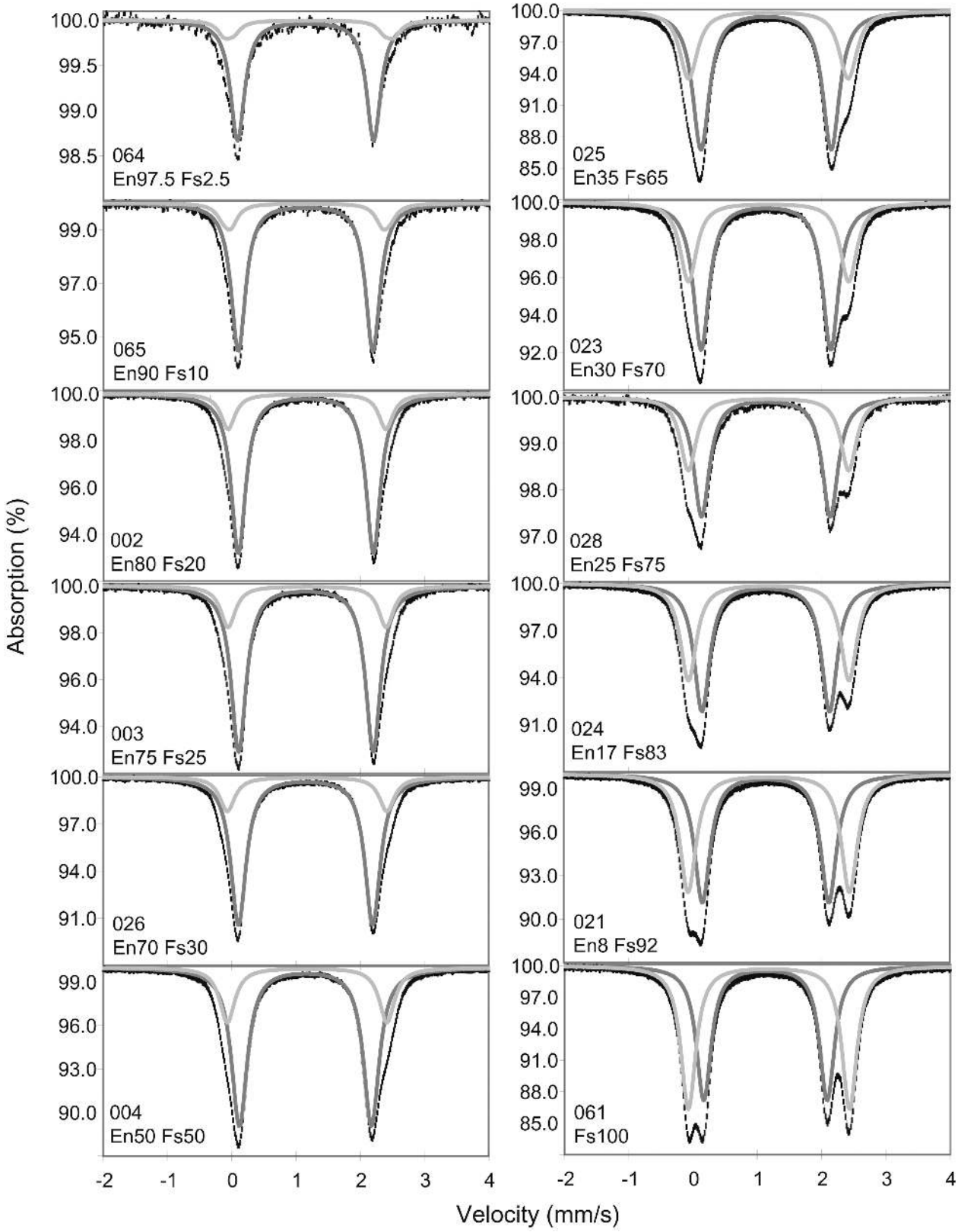

Fig. 2. Mössbauer spectra and modeled fits for the synthetic pyroxenes. Data points are shown with error bars representing the standard measurement error. The modeled fit is displayed as a thin black line, with the component doublet attributed to the M1 site displayed in light gray and the M2 doublet shown in dark gray.

formula unit (pfu). It is likely that the origin of Fe^{3+} in En_{100} is very minor impurities in the starting materials for synthesis or trace contamination during grinding of powders between synthesis runs.

Near-Infrared Spectroscopy

Near-infrared spectra of the synthetic pyroxenes are presented in Fig. 1b. In the near-infrared, the spectra are characterized by two absorption bands near 1 and 2 μm. Crystal field theory predicts that when Fe^{2+} resides in either octahedral site, the higher energy e_g orbital will be split, resulting in absorption of light at two energies (Burns 1993). Fe^{2+} in the larger, more distorted M2 site produces a prominent band at 1 μm. However, a weaker absorption due to Fe^{2+} in the more symmetric M1 site is centered at very near the same energy (within ~50 cm^{-1}) (Burns 1993). In contrast, the observed 2 μm absorption is due only to Fe^{2+} in the M2 site. This combination accounts for the difference in band depth between the 1 and 2 μm bands, as the deeper 1 μm absorption is actually a composite of two nested absorptions from the M1 and M2 sites, while the 2 μm band is due strictly to Fe^{2+} in the M2 site. As has been previously observed, the 1 and 2 μm absorptions shift to longer wavelengths with increasing total iron content (e.g., Adams 1974; Cloutis and Gaffey 1991a). The second absorption caused by Fe^{2+} in the M1 site is centered near 1.2 μm, on the shoulder of the 1 μm band. Pure enstatite exhibits no strong 1 and 2 μm absorptions because there is virtually no absorbing species (Fe^{2+}). However, the small (0.06%) amount of iron for En_{100}, present as both Fe^{2+} and Fe^{3+}, affects the slope of the spectrum at visible wavelengths.

Fe^{2+} prefers the M2 site in Ca-free pyroxenes because it is larger than the M1 site and the Fe^{2+}-O bonds of the M2 site have a slightly more covalent character than those of the M1 site (e.g., Ghose 1965; Burns 1993). The extent of preference between the M2 and M1 sites in a simple Mg-Fe^{2+} system depends primarily on equilibration temperature, though previous studies of both natural and synthetic orthopyroxenes reveal that some portion of Fe^{2+} is still found in the M1 site (e.g., Virgo and Hafner 1970; Saxena and Ghose 1971).

Modeling Individual Absorptions with the Modified Gaussian Model

To provide a quantitative analysis of the variations in near-infrared absorption features, we have decomposed each spectrum into a continuum slope and several modified Gaussian curves. The MGM fits are presented in Fig. 4. Although the 1 μm absorption band is actually a composite absorption with contributions from both the M1 and M2 sites, the energies of the two transitions are within roughly 50 cm^{-1} of one another. For simplicity, we modeled this feature with one absorption band. In Fig. 4, the 1 μm M1 + M2 band and the 2 μm M2 band are displayed in black and the 1.2 μm M1 band is displayed in gray. The pyroxene containing the lowest amount of total iron (2.5%) exhibits a weak but unassigned absorption near 2.2 μm, probably due to phyllosilicate contamination (Fig. 1b). This sample has been retained in our band position analyses, as this absorption does not coincide with the positions of the pyroxene crystal field bands. However, MGM fits for this sample required that both the slope and offset of the continuum were held constant. As this affects the relative bands areas, we have excluded this sample from band area analyses.

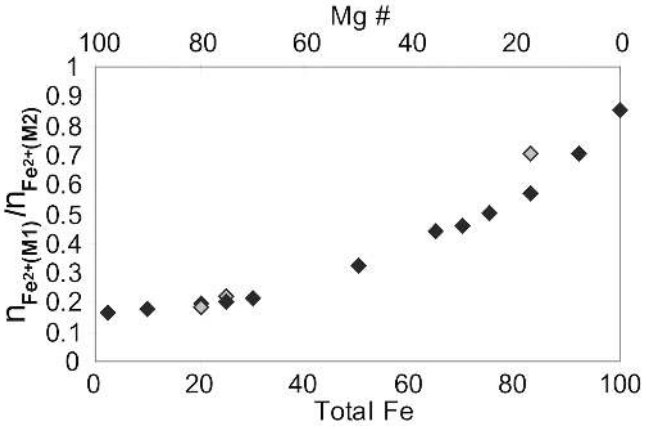

Fig. 3. The calculated relative site populations of Fe^{2+} as a function of total Fe content and Mg number. Duplicate pyroxenes at 20, 25, and 83% total iron are shown as gray diamonds.

Final model parameters of the MGM fits to the near-infrared spin-allowed crystal field absorption bands are presented in Table 6. Several general trends are apparent. As shown in Fig. 5, the band centers of all three spin-allowed crystal field bands shift to longer wavelengths with increasing total iron content. The positions of the band centers are related to the energies of the crystal field transitions, and controlled by the geometry and size of the cation site in the ligand field (Burns 1993). Thus, the movement of the band centers is primarily due to the change in cell parameters as the larger Fe^{2+} cation is incorporated into the pyroxene.

The intensity of an absorption band is controlled by several factors, including the concentration of the absorbing species (in this case Fe^{2+}) and the asymmetry of the site (Burns 1993). Because the M2 site is much less symmetrical than the M1 site, crystal field absorption bands caused by Fe^{2+} in the M2 site are higher in intensity than those due to Fe^{2+} in the M1 site. The 1 μm band is more intense than the 2 μm band because of the superposition of the M1 and M2 absorptions at that energy. The model fits to the high (≥50%) total iron pyroxenes all show a symmetrical RMS error, centered at the middle of each of the spin-allowed crystal field absorptions. Although this error is minimal, it suggests that the bands are saturated (Sunshine and Pieters 1993).

Band intensity was used to examine relative changes in Fe^{2+} distribution between the M1 and M2 crystallographic

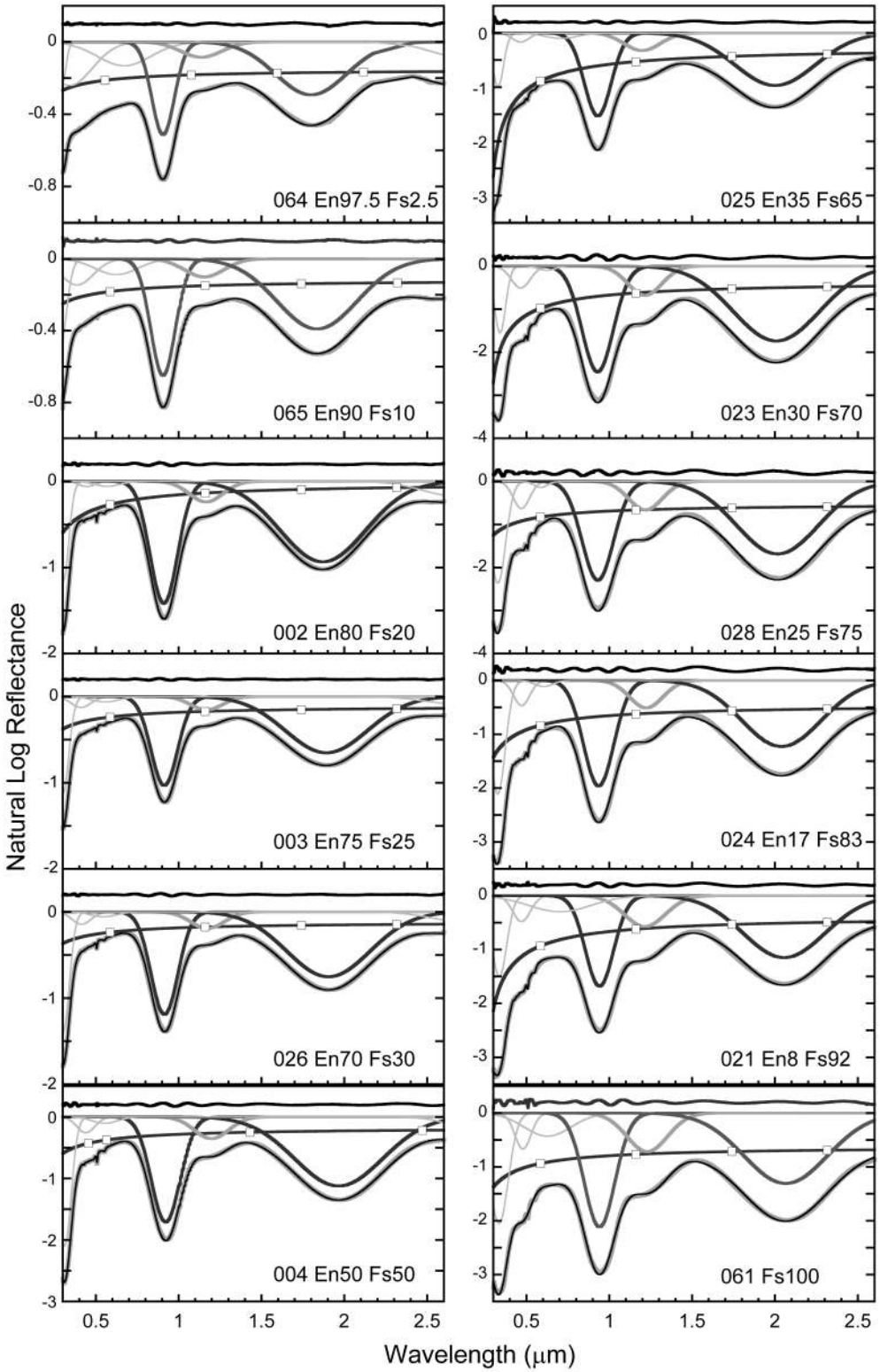

Fig. 4. MGM fits of synthetic pyroxene vis-NIR spectra. Spectra are shown as a thick gray line; the composite fit is displayed as a thin black line superposed on the data. The continuum is directly above the data and is shown as a black line with square symbols. The continuum-free component modified Gaussian curves are separated into light gray (charge transfer bands), black (spin-allowed crystal field, M2 site), and medium gray (spin-allowed crystal field, M1 site). The black line above the zero line represents the RMS error in the fit as a function of wavelength.

Table 6. The final model parameters of MGM fits to 5 nm resolution spectra of synthetic orthopyroxenes.

		1 μm: Fe^{2+} in M1 and M2					1.2 μm: Fe^{2+} in M1					2 μm: Fe^{2+} in M2				
Sample	Fe	Center	FWHM	Intensity	$NI_{1\ \mu m}$	Area	Center	FWHM	Intensity	$NI_{1.2\ \mu m}$	Area	Center	FWHM	Intensity	$NI_{2\ \mu m}$	Area
064	2.5	906	160	–0.51	0.58	32	1136	290	–0.08	0.09	10	1799	504	–0.29	0.33	58
065	10	906	174	–0.65	0.57	31	1152	276	–0.10	0.09	8	1833	568	–0.39	0.34	61
002	20	910	194	–1.42	0.55	30	1166	237	–0.24	0.09	6	1870	609	–0.93	0.36	63
003	25	913	187	–1.03	0.56	32	1168	225	–0.15	0.08	6	1892	583	–0.65	0.35	63
026	30	914	190	–1.19	0.56	32	1173	236	–0.19	0.09	6	1904	591	–0.75	0.35	62
004	50	922	202	–1.71	0.54	31	1195	242	–0.35	0.11	8	1963	624	–1.12	0.35	62
025	65	931	191	–1.53	0.54	31	1199	255	–0.32	0.12	9	2001	573	–0.97	0.34	60
023	70	930	222	–2.46	0.50	31	1215	240	–0.68	0.14	9	2008	611	–1.74	0.36	60
028	75	931	223	–2.30	0.49	31	1218	237	–0.67	0.14	10	2016	582	–1.69	0.36	59
024	83	936	216	–1.96	0.53	34	1223	235	–0.51	0.14	10	2040	563	–1.23	0.33	56
021	92	941	200	–1.68	0.49	29	1214	291	–0.57	0.17	14	2055	582	–1.15	0.34	57
061	100	940	222	–2.12	0.52	34	1231	275	–0.68	0.17	13	2065	577	–1.27	0.31	53

Area has been normalized to sum to 100 for the 1, 1.2, and 2 μm bands; $NI_{1\ \mu m} = Intensity_{1\ \mu m}/(Intensity_{1\ \mu m} + Intensity_{1.2\ \mu m} + Intensity_{2\ \mu m})$; $NI_{1.2\ \mu m} = Intensity_{1.2\ \mu m}/(Intensity_{1\ \mu m} + Intensity_{1.2\ \mu m} + Intensity_{2\ \mu m})$; $NI_{2\ \mu m} = Intensity_{2\ \mu m}/(Intensity_{1\ \mu m} + Intensity_{1.2\ \mu m} + Intensity_{2\ \mu m})$.

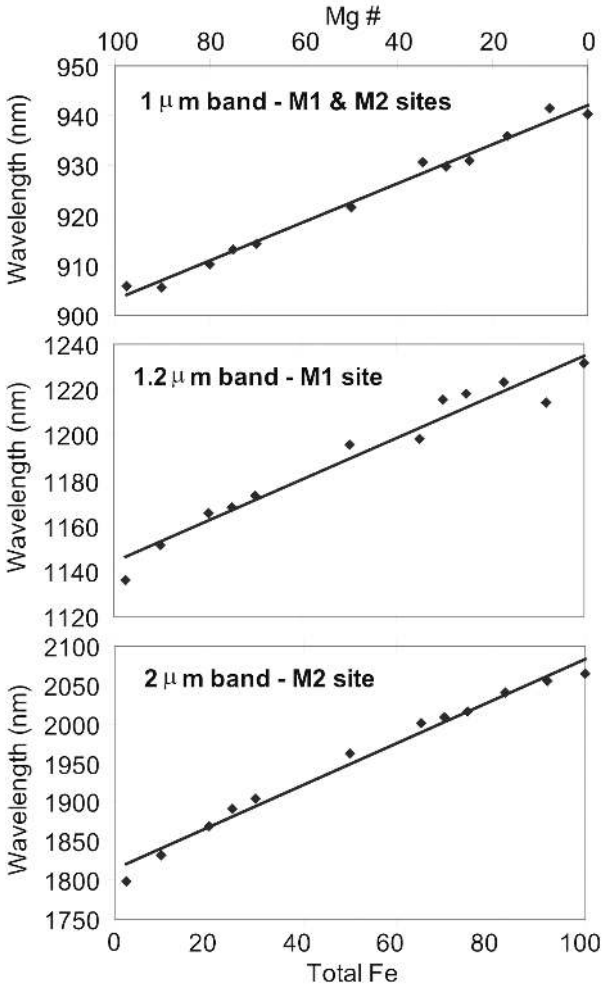

Fig. 5. The movement of spin-allowed crystal field absorption band centers with increasing total iron content and decreasing Mg number.

sites. To accentuate the differences between the intensities of absorption bands in a pyroxene of a given total iron content, we have normalized the intensity of each band relative to the sum of the intensities of the three bands ($NI_{1\ \mu m}$, $NI_{1.2\ \mu m}$, and $NI_{2\ \mu m}$ in Table 6). The normalized intensity of the 1 μm band, which reflects contributions from Fe^{2+} in both the M1 and M2 sites, remains almost constant across the suite of pyroxenes, ranging from 49–58%. This percentage decreases slightly for higher iron pyroxenes, further suggesting that these 1 μm bands are saturated. The normalized intensity of the 1.2 μm M1 band is mostly constant until the pyroxenes reach 50% Mg, 50% Fe^{2+}, at which point the intensity progressively increases. Like the 1 μm band, the normalized intensity of the 2 μm band remains roughly constant over the full suite of pyroxenes.

Comparison of Mössbauer-Derived Cation Site Populations with NIR Absorption Bands

It has been shown previously that polarized transmission mode infrared absorption spectra of orthopyroxene crystals can be used to quantitatively determine the concentration of Fe^{2+} in the M1 and M2 crystallographic sites (Goldman and Rossman 1979). The methods described depend strongly on the thickness of the sample and the orientation of the orthopyroxene crystal, and cannot be directly applied to reflectance spectra of bulk samples comprised of many randomly oriented orthopyroxene grains. It may, nevertheless, be possible to estimate the relative proportions of Fe^{2+} in the M1 and M2 sites using band area ratios (Besancon et al. 1991; Burns et al. 1991), or the related band intensity ratios. Burns and Besancon found that when two pyroxenes were heated to a series of different temperatures, the disorder (increased amount of Fe^{2+} in the M1 site) measured by the change in relative areas of the M1 and M2 Mössbauer doublets was linearly related to the change in the area of the 1.2 μm band divided by the sum of the areas of the 1.2 μm and 2 μm bands. Such a method relies only on the assumption that the reflectance spectrum represents an average of a large number of randomly oriented grains (i.e., that the spectrum is not dominated by the spectrum of one particular crystallographic axis).

A comparison of the MGM derived band areas for the 1.2 μm and 2 μm bands with the doublet areas for the M1 and M2 doublets as measured by Mössbauer is presented in Fig. 6. Our results also reveal a generally linear trend, as observed by Burns et al. (1991). Because band width, which is sensitive to factors other than mineral chemistry (i.e., temperature), is incorporated into band areas, it may be better to use band intensity for comparisons with Mössbauer data. In Fig. 7, the ratio of the 1.2 μm band intensity to the sum of the intensities of the 1.2 and 2 μm bands is plotted as a function of the Mössbauer-derived concentration of Fe^{2+} in the M1 and M2 sites. These data display a similar but stronger correlation than seen between the Mössbauer data and relative band areas.

Visible Spectroscopy

High-resolution visible spectra of the synthetic pyroxene suite are shown in Figs. 1c and 8. The strongest discernible spin-forbidden absorption feature occurs near 506 nm. Absorptions near 425 and 550 nm are also apparent. With increasing Fe content, additional bands between roughly 450–490 nm become more prominent. These three weak, bands are often difficult to discern from one another, though at higher iron contents the three peaks are well-defined. This is consistent with previous transmission measurements of synthetic ferrosilite by Hazen et al. (1978), which reveal a band centered at 480 nm with two prominent shoulders.

Modeling of Visible Wavelength Absorption Bands Using MGM

Modeled fits of the high-resolution visible spectra are presented in Fig. 8. The MGM is used primarily to determine band position and total number of the spin-forbidden features,

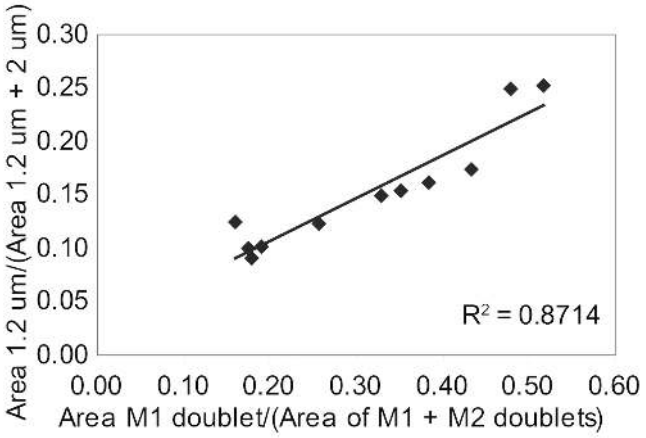

Fig. 6. The relationship between the band areas derived for the 1.2 and 2 μm bands compared with the Mössbauer derived M1 and M2 doublet areas.

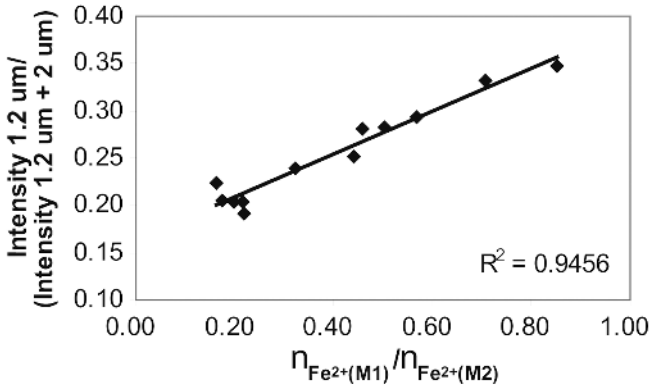

Fig. 7. Comparison of the 1.2 μm and 2 μm band intensity ratios with the ratio of the concentration of Fe^{2+} in the M1 and M2 sites as calculated from Mössbauer data.

as the band areas, widths, and intensities are highly dependent on the placement of the continuum and charge transfer bands. The RMS error in the region near the 506 nm band is systematically higher than at other wavelengths and may suggest that there are smaller absorptions on either side of this feature. This could either be a result of the shape of the modified Gaussian curve not describing the spin-forbidden absorption exactly, or there could be additional, weak absorptions around this band. The RMS error pattern near the 506 nm band does not change systematically with chemistry. Until we resolve whether the error pattern is due to band shape or band multiplicity, we have chosen to model this as a single absorption.

The derived band centers for the spin-forbidden absorption bands are given in Table 7. Although all modeled absorption features trend towards longer wavelengths with increasing iron content, the movement of the absorption features centered near 425 and 506 nm is the most systematic. The movement of the 506 nm absorption band center with increasing Fe content is illustrated in Fig. 9. The movement of the remaining features is less distinctive, and may reflect changes in relative intensities of composite bands. In pyroxenes with less than 75% total iron, only five spin-forbidden absorption bands were necessary to model the spectrum.

DISCUSSION

Spin-Allowed Crystal Field Transitions

1 and 2 μm Bands

The systematic shifting of the 1 and 2 μm bands in our data is consistent with previously observed trends for orthopyroxenes. Figure 10 shows a plot of the wavelength of the MGM-derived (continuum removed) band centers for the 1 and 2 μm absorption bands compared with data for pyroxenes reported by Adams (1974) and Cloutis and Gaffey (1991a). The synthetic pyroxenes clearly lie within the cloud of natural orthopyroxenes, though they define a much tighter trend than previously observed.

Unlike previous measurements of natural pyroxenes, our results are explicitly related to changes in Fe^{2+} content with all other chemical variables held constant. The trend defined by the synthetic pyroxenes provide a baseline for how a pyroxene spectrum varies as the slightly larger Fe^{2+} cation substitutes for Mg. Though both terrestrial and extraterrestrial pyroxenes almost undoubtedly contain other cations, and therefore may diverge from this trend, we can use the deviations and our understanding of the crystal structure to predict what other cations are present. For example, if the positions of the 1 and 2 μm bands of a pyroxene plot well below this trend, they are likely to contain a cation smaller than Mg, such as Al^{3+}, resulting in a smaller average radius of the M1 (and possibly M2) site and thus a greater crystal field splitting. Similarly, the presence of a larger cation, such as Ca, will cause a pyroxene to plot further to the right and above one of a similar Mg-Fe ratio that is Ca-free. As illustrated in Fig. 10, a natural enstatite with 1% Al_2O_3, <0.5% CaO, and 12.9% total iron (enstatite from Webster, North Carolina, USA, RELAB ID PE-CMP-030, open triangle) plots along the trend defined by the synthetic Ca-free pyroxenes, just to the right of the 10% total iron synthetic pyroxene, while a hypersthene measured by Nash and Conel (1974) containing 4.32% Al_2O_3 (open square) plots below and towards the left of the trend.

1.2 μm Band

A 1.2 μm band is required for a good fit for all of our pyroxenes, and is prominent in all pyroxenes with 20% or more total iron. The intensity of the 1.2 μm band increases consistently with increasing iron content, and similarly to the 1 and 2 μm bands, the 1.2 μm band shifts to longer wavelengths with increasing total iron. Both the 2.5% and 10% total iron samples exhibit a weak, flat band near 1.2 μm. The flatness of these bands cause their band widths to be

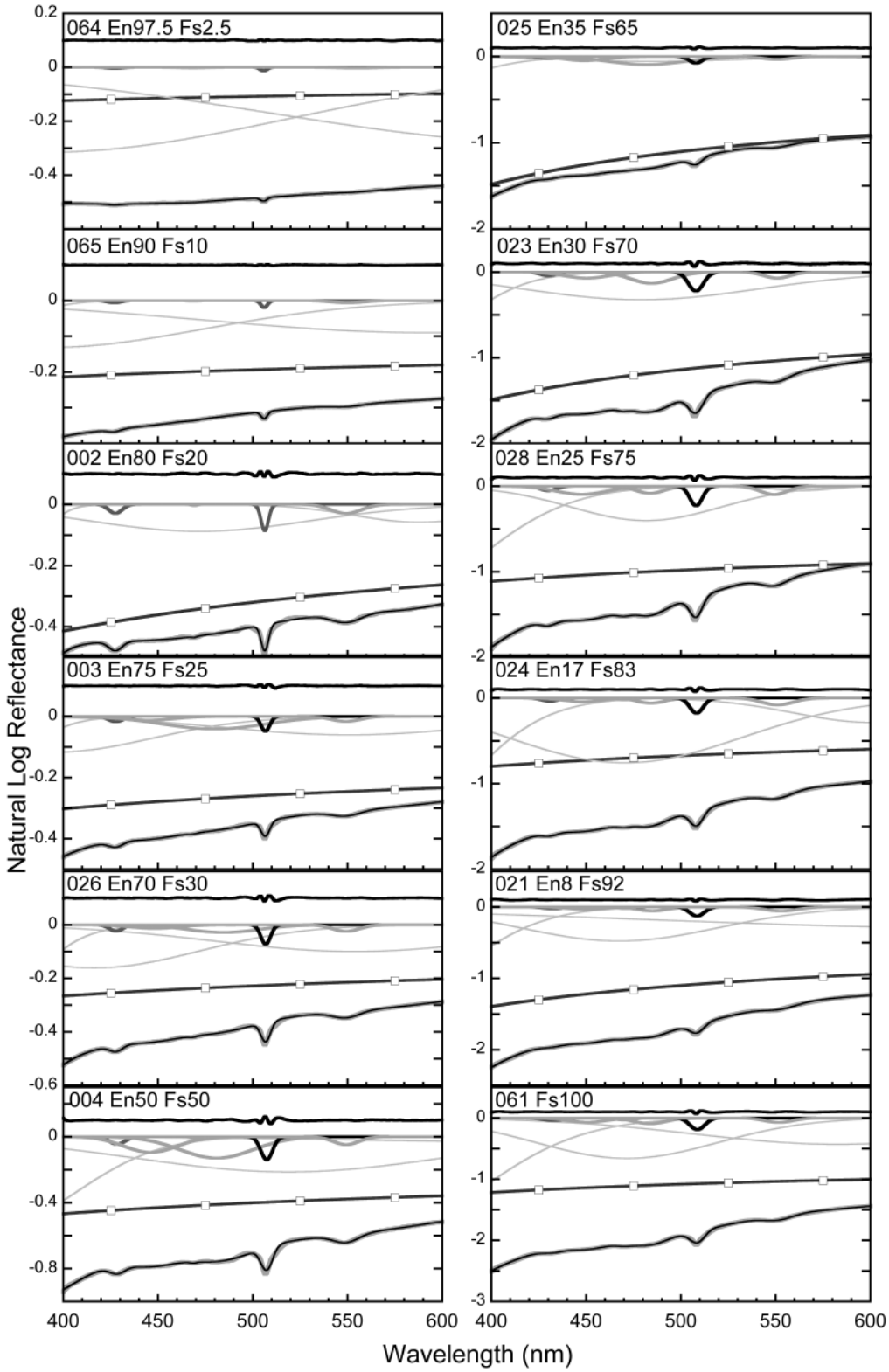

Fig. 8. MGM fits of high-resolution (0.5 nm) visible wavelength synthetic pyroxene spectra. Spectra are shown as a thick gray line, with the composite fit displayed as a thin black line superposed on the data. The continuum is directly above the data and is shown as a black line with square symbols. The continuum-free component modified Gaussian curves are separated into thin gray (charge transfer bands), black (spin-forbidden crystal field, M2 site) and medium thick gray (spin-forbidden crystal field, M1 site). The black line above the zero line represents the RMS error in the fit as a function of wavelength.

Table 7. MGM-derived band centers for 0.5 nm resolution visible wavelength spectra.

Sample	Fe	Wavelength of band center (nm)					
064	2.5	427.1	n.a.[a]	468.4	n.a.[a]	505.8	555.1
065	10	426.9	n.a.[a]	468.6	n.a.[a]	506.1	550.2
002	20	427.5	n.a.[a]	469.2	n.a.[a]	506.4	549.3
003	25	427.7	445.0	468.7	479.8	506.7	549.2
026	30	427.9	448.2	468.4	484.6	506.9	549.3
004	50	428.4	446.1	468.7	480.9	507.4	549.3
025	65	430.7	449.0	469.2	482.1	508.0	550.7
023	70	430.1	450.3	470.0	484.6	508.0	550.9
028	75	430.0	447.7	470.0	483.8	508.0	549.2
024	83	431.0	447.8	470.2	484.2	508.3	551.0
021	92	432.4	450.7	470.6	484.9	508.5	553.0
061	100	432.7	450.7	470.2	483.8	508.7	551.7

[a]Low-iron spectra only required four bands to produce a good fit.

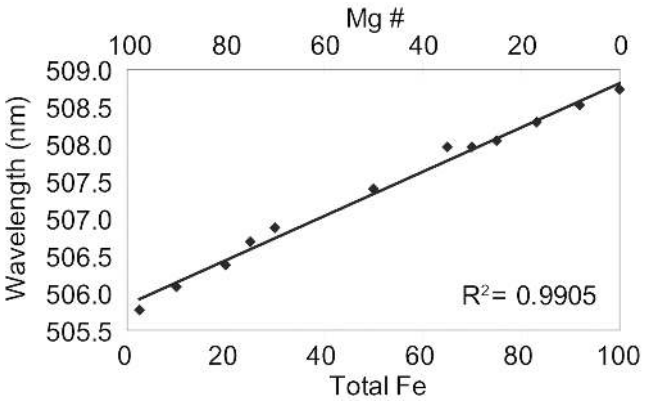

Fig. 9. The movement of the 506 nm spin-forbidden absorption band with total iron content and Mg number.

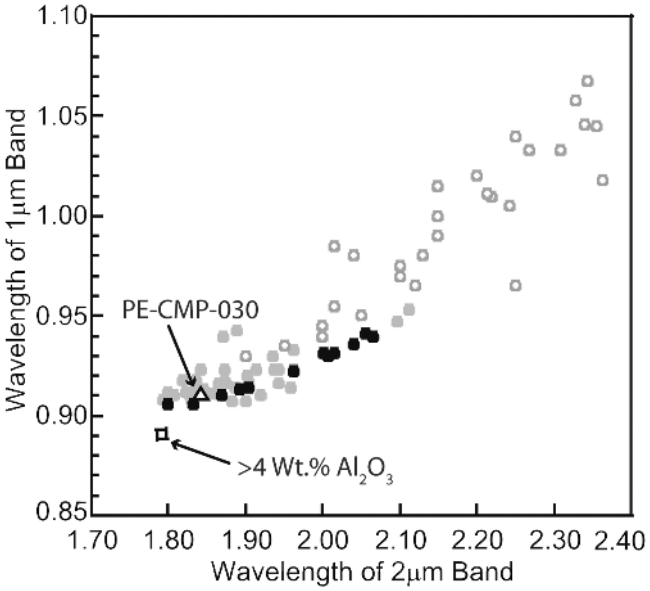

Fig. 10. The MGM-derived wavelength positions of the 1 and 2 μm band centers for the synthetic orthopyroxenes compared to previous data for pyroxene band minima collected by Adams (1974) and Cloutis and Gaffey (1991a). Synthetic pyroxenes are shown as closed black circles, natural orthopyroxenes are displayed as closed gray circles, and clinopyroxenes are displayed as open gray circles. Natural enstatite from Webster, North Carolina, USA, is displayed as an open triangle, and a natural hypersthene measured by Nash and Conel (1974) is shown as an open square.

highly dependent on the placement of the continuum curve. Although the derived band centers still appear to lie along the trend observed for the rest of the series (Fig. 5), the band areas are several percent larger than anticipated due to their disproportionately large widths (Table 6).

Mössbauer data confirm that the lowest iron synthetic pyroxenes in our series contain a slightly larger proportion of iron in their M1 sites than most terrestrial pyroxenes of similar iron content. Figure 11 compares three of the synthetic pyroxenes with natural orthopyroxenes of similar Mg-Fe ratio. As is illustrated in Fig. 11, the spectrum of PE-CMP-030, which has nearly 13% total iron, does not visibly show a distinctive feature with the same character at 1.2 μm. However, when the continuum of PE-CMP-030 is modeled using the MGM, a band is necessary at that wavelength. The variability between the visual appearance of the 1.2 μm region of the synthetic pyroxenes and the terrestrial enstatite represent a difference in iron content in the M1 site, primarily due to differences in the closure temperature of either sample. The synthetic pyroxenes represent an equilibrium cation ordering between the M1 and M2 sites at their synthesis temperatures, near 900 °C, while PE-CMP-030, separated from a highly metamorphosed peridotite, experienced much cooler metamorphic temperatures. Studies of order-disorder in orthopyroxenes have shown that at increasingly higher temperatures, the higher vibrational energy of the mineral lattice allows Fe^{2+} and Mg to exchange more freely and Fe^{2+} to occupy either the M1 or the M2 site with less preference for the larger M2 site (e.g., Virgo and Hafner 1970; Saxena and Ghose 1971). Pyroxenes quenched or cooled quickly at igneous temperatures, including many extraterrestrial samples, preserve this disorder (e.g., Pollack 1968; Virgo

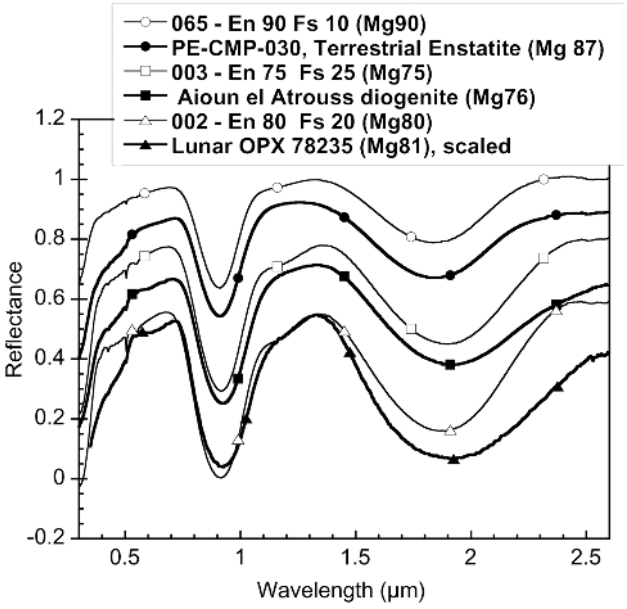

Fig. 11. A comparison of several synthetic pyroxenes (thin black) with terrestrial and extraterrestrial orthopyroxenes of similar Mg numbers (thick black). Data have been offset for clarity. Lunar OPX 78235 is of much lower albedo than the other samples and has thus been scaled to synthetic pyroxene 002 for comparison of features. The 1.2 μm band, present in both the lunar OPX and the diogenite, is not visually distinctive in the terrestrial enstatite. Note that the lunar OPX contains 3.2 wt% CaO and thus the band centers of the 1 and 2 μm bands are shifted to longer wavelengths than the comparable synthetic pyroxene.

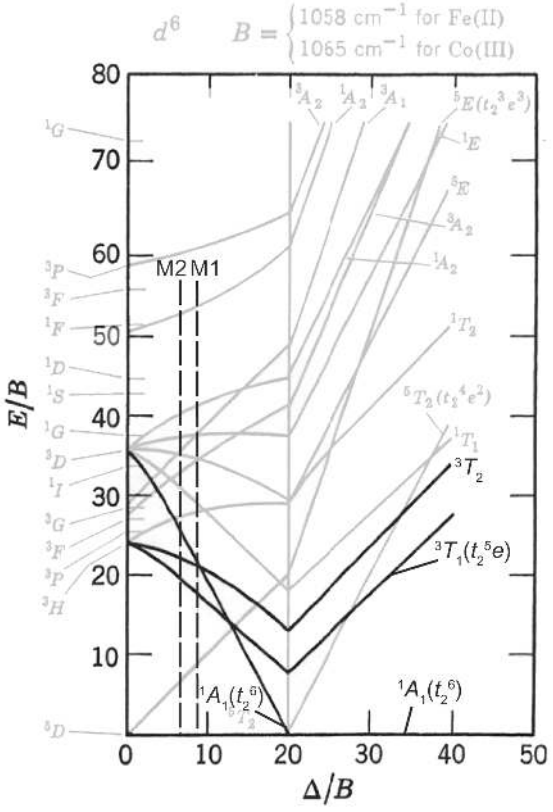

Fig. 12. Tanabe-Sugano diagram for a d^6 cation in an octahedral crystal field. Adapted from Cotton (1963). The two vertical dashed lines represent the two octahedral sites for orthopyroxene.

1973; Molin et al. 1991). Pyroxenes that are cooled at slower temperatures or reheated during metamorphic events show greater degrees of ordering of Fe^{2+} into the M2 sites, as it prefers to reside in the larger M2 site in a cooler, more rigid lattice. This ordering of Fe^{2+} between the pyroxene crystallographic sites represents a balance between the strain in the lattice and the kinetics necessary to reorder the cations, and has thus been used as a geospeedometer.

Determining M1 and M2 Site Occupancy from Near-Infrared Spectra

The possibility of determining M1 and M2 site occupancy from reflectance data introduces exciting possibilities for remote sensing applications. The correlations between the site occupancy determined by Mössbauer spectroscopy with the areas of the 1.2 μm and 2 μm bands for this data set (Fig. 6), and in the work done by Burns and Besancon (Besancon et al. 1991; Burns et al. 1991) are compelling, but cannot yet be used to quantitatively extract site populations from reflectance data. As described above, the band area of a weak 1.2 μm band is dependent on the placement of the continuum, which, in natural samples, is nontrivial. Space weathering, charge transfers between cations of different valences, and scattering effects are among many issues that may affect the continuum slope of a reflectance spectrum. Using the relative intensity of the 1.2 and 2 μm bands instead of band area addresses some complications and will be tested further using samples from a variety of thermal histories. In darker samples, band saturation may also complicate issues, as the stronger 2 μm band would saturate before the 1.2 μm band, affecting the band area or intensity ratio. Nevertheless, a strong 1.2 μm absorption is a good qualitative indication that a pyroxene cooled rapidly from igneous temperatures (perhaps at a surface), whereas a weak 1.2 μm absorption indicates that the pyroxene cooled slowly (perhaps at a deeper depth) or re-equilibrated at closer to metamorphic temperatures.

Spin-Forbidden Bands in Fe^{2+}-Bearing Pyroxenes

Distinct spin-forbidden bands are observed in our pyroxene spectra at visible wavelengths. Although many spin-forbidden transitions are possible, only 2–3 electronic configurations occur at energies within the visible for each cation site. Higher energy transitions which occur in the ultraviolet are most likely obscured by very strong metal-oxygen charge transfer absorption bands at similar wavelengths.

Figure 12 is a Tanabe-Sugano diagram for a d^6 cation (such as Fe^{2+}) in an octahedral crystal field. Tanabe-Sugano diagrams can be used to estimate the energies at which spin-forbidden and spin-allowed absorption bands will occur in spectra. Spin-forbidden transitions that occur in the visible are highlighted by dark lines in Fig. 12. Because of the differing environments surrounding the M1 and M2 octahedral sites, six distinctive spin-forbidden transition energies are observed in our pyroxene spectra, rather than three. The two vertical dashed lines labeled M1 and M2 in Fig. 12 represent the approximate predictions for the two octahedral sites of orthoferrosilite, calculated using the Racah *B* parameter of 1058 cm^{-1} from Cotton (1963) and the crystal field splitting (Δ) values for orthoferrosilite from Burns (1993). Based on this diagram, the order of spin-forbidden lines, from E/*B* of 15 (15,870 cm^{-1} or 630 nm) through E/*B* of 26 (27,508 cm^{-1} or 364 nm) is: $^3T_{1g}$(M1), $^3T_{1g}$(M2), $^3T_{2g}$(M1), $^1A_{1g}$(M1), $^3T_{2g}$(M2), $^1A_{1g}$(M2). Depending on the exact Δ and *B* of any specific pyroxene, the order of the $^1A_{1g}$(M1) and $^3T_{2g}$(M2) transitions might reverse.

Using this predicted band order, we can begin to assign the visible wavelength absorption bands measured for our spectra to the spin-forbidden transitions and crystallographic sites associated with them. Because this pyroxene suite varies only in Fe^{2+} content, we can also test these assignments by looking at the band strengths for pyroxenes of higher or lower total iron content. The first spin-forbidden transition recorded by our spectra occurs near 550 nm. This is consistent with the energy predicted for the $^3T_{1g}$ transition in the M1 site. The $^3T_{1g}$ transition for the M2 site occurs at a slightly higher energy, and is most likely responsible for the strongest visible wavelength band centered near 506 nm. A group of 3 weak absorption bands, which is centered near 470 nm, may be a composite band associated with the $^3T_{2g}$ transition for the M1 site. The remaining absorption that is clearly discernible in our pyroxene data occurs at ~430 nm, near the energy at which the $^3T_{2g}$ transition for the M2 site is predicted to occur. If these tentative assignments are correct, only the 506 and 430 nm absorption bands, which are both associated with the M2 site, should be prominent in the low iron pyroxenes. Indeed, in pyroxene 064, containing 2.5% total iron, only these two features are present. The bands associated with the M1 site appear first in pyroxene 002, which contains 20% total iron, and become stronger with increasing total iron content.

The most marked difference between these band assignments and those made by previous authors (as summarized in Table 1) is in the composite absorption centered near 470 nm. A broad band centered at near this wavelength has been previously attributed to Ti^{3+} (Burns et al. 1972, 1973). As the synthetic pyroxenes are titanium free, we are confident that Fe^{2+} can produce the observed absorptions. The synthetic ferrosilite measured in transmission by Hazen (1978) also displays a strong triplet absorption feature at this wavelength. While it is possible that Ti^{3+} may produce an absorption at a similar wavelength, bands that occur at this wavelength cannot be used to definitively diagnose the presence of titanium in a pyroxene, as it coincides with the iron absorption.

CONCLUSIONS

Measurement and analysis of synthetic Mg-Fe^{2+} pyroxenes allows quantitative characterization of how crystal chemistry controls reflectance spectra over a range of chemistries not necessarily accessible on Earth. This information provides a critical baseline for analysis of both terrestrial and extraterrestrial pyroxene spectra. We focus in this work on calcium-free pyroxenes to isolate how changes in iron and magnesium content affect a pyroxene spectrum. The diagnostic crystal field absorption bands of these high-purity pyroxenes exhibit well-defined trends in the visible and near-infrared, which are directly linked to their chemistry and site occupancy. The systematic movement of the 1 and 2 μm absorption bands of the synthetic orthopyroxene series defines a much tighter trend than that documented previously for natural pyroxenes, allowing us to quantitatively document how substitution between Mg and Fe^{2+} in the crystal lattice changes a pyroxene spectrum. Several additional key results have emerged:

1. A crystal field absorption band due to Fe^{2+} in the M1 crystallographic site is explicitly verified at 1.2 μm in all Ca-free synthetic pyroxenes, implying that Fe^{2+} exists in the M1 site even for low-iron, calcium-free pyroxenes. Like the 1 and 2 μm bands, this feature moves to longer wavelengths with increasing total iron. In addition, the 1.2 μm band intensifies as the total iron (and iron in the M1 site) increases. Unlike pyroxenes on Earth, which have often undergone extensive metamorphism since their emplacement, many pyroxenes in the solar system cooled rapidly from igneous temperatures and are likely to show a strong degree of disorder (and therefore a stronger 1.2 μm pyroxene absorption). The data for this pyroxene series highlight the importance of the 1.2 μm band, and indicate that most observations of a 1.2 μm band in conjunction with the two M2 pyroxene bands are the result of Fe^{2+} in the M1 site. Alternate interpretations as plagioclase or olivine species are unnecessary.
2. The relative 1, 1.2, and 2 μm band areas and intensities provide information about both the total iron content of a pyroxene and the relative proportion of iron in the M1 and M2 sites. These relationships can be used as constraints for modeling pyroxene spectra and may be useful in estimating the extent of Mg-Fe^{2+} ordering between the M1 and M2 sites.
3. At visible wavelengths, a series of spin-forbidden crystal field absorptions produced by Fe^{2+} in the M1 and M2 sites are clearly identified. Based on predicted energies

for iron in octahedral coordination, bands at 425 nm and 506 nm bands are attributed to Fe^{2+} in the M2 site. The 506 nm band moves to longer wavelengths with increasing total iron content (~3 nm movement). An absorption near 550 nm and a weak composite absorption feature centered near 470 nm are attributed to Fe^{2+} in the M1 site. None of the absorptions attributed to Fe^{2+} in the M1 site shift significantly with total iron content.

Investigations of an expanded series of calcium-bearing synthetic pyroxenes is ongoing to further constrain the behavior of visible and near-infrared absorption features in a chemically defined system. The combined suite will allow characterization of diagnostic absorption features of both orthopyroxenes and clinopyroxenes throughout the pyroxene quadrilateral.

Acknowledgments–Many thanks to Ed Cloutis and Jessica Sunshine, whose thoughtful reviews helped improve this work significantly. We are extremely grateful to Don Lindsley and Al Turnock for providing us these pyroxene samples. We thank Taki Hiroi for his dedication and care in measuring these samples in RELAB, Joe Devine for his assistance with EMP measurements, and Eli Sklute and Yarrow Rothstein for their help with fitting Mössbauer spectra. Partial support for this project was provided by NASA grants NNG04GG12G and NNG04GB53G, UCLA subcontract 2090 FFC198 of NASA grant NNM05AA86C, and NSF grant EAR-0439161.

Editorial Handling—Dr. Beth Ellen Clark

REFERENCES

Adams J. B. 1974. Visible and near-infrared diffuse reflectance spectra of pyroxenes as applied to remote sensing of solid objects in the solar system. *Journal of Geophysical Research* 79:4829–4836.

Anovitz L. M., Essene E. J., and Dunham W. R. 1988. Order-disorder experiments on orthopyroxene: Implications for the orthopyroxene geospeedometer. *American Mineralogist* 73: 1060–1073.

Bancroft G. M. 1969. Quantitative site populations in silicate minerals by the Mössbauer effect. *Chemical Geology* 5:255–258.

Bancroft G. M., Burns R. G., and Howie R. A. 1967. Determination of the cation distribution in the orthopyroxene series by the Mössbauer effect. *Nature* 213:1221–1223.

Besancon J. R. 1981. Rate of cation disordering in orthopyroxenes. *American Mineralogist* 66:965–973.

Besancon J. R., Burns R. G., and Pratt S. F. 1991. Reflectance spectra of Fe^{2+}-Mg^{2+} disordered pyroxenes: Implications to remote-sensed spectra of planetary surfaces (abstract). 22nd Lunar and Planetary Science Conference. p. 95.

Bibring J. P., Langevin Y., Gendrin A., Gondet B., Poulet F., Berthe M., Soufflot A., Arvidson R., Mangold N., Mustard J., Drossart P., Erard S., Forni O., Combes M., Encrenaz T., Fouchet T., Merchiorri R., Belluci G., Altieri F., Formisano V., Bonello G., Capaccioni F., Cerroni P., Coradini A., Fonti S., Kottsov V., Ignatiev N., Moroz V., Titov D., Zasova L., Pinet P., Douté S., Schmitt B., Sotin C., Hauber E., Hoffmann H., Jaumann R., Keller U., Duxbury T., and Forget F. 2005. Mars surface diversity as revealed by the OMEGA/Mars Express observations. *Science* 307:1576–1581.

Burnham C. W., Ohashi Y., Hafner S. S., and Virgo D. 1971. Cation distribution and atomic thermal vibrations in an iron-rich orthopyroxene. *American Mineralogist* 56:850–876.

Burns R. G. 1993. *Mineralogical applications of crystal field theory.* Cambridge: Cambridge University Press. 551 p.

Burns R. G., Parkin K. M., Loeffler B. M., Leung I. S., and Abu-Eid R. M. 1967. Further characterization of spectral features attributed to titanium on the moon. Proceedings, 7th Lunar Science Conference. pp. 2561–2578.

Burns R. G., Huggins F. E., and Abu-Eid R. M. 1972. Polarized absorption spectra of single crystals of lunar pyroxenes and olivines. *Earth, Moon, and Planets* 4:93–102.

Burns R. G., Vaughan D. J., Abu-Eid R. M., and Witner M. 1973. Spectral evidence for Cr^{3+}, Ti^{3+}, and Fe^{2+} rather than Cr^{2+} and Fe^{3+} in lunar ferromagnesian silicates. Proceedings, 4th Lunar Science Conference. pp. 983–994.

Burns R. G., Besancon J. R., and Pratt S. F. 1991. Reflectance spectra of Fe^{2+}-Mg^{2+} disordered pyroxenes: Implications to remote-sensed spectra of planetary surfaces. NASA Report #N92-10823. Washington, D.C.: NASA. pp. 253–255.

Cloutis E. A. 2002. Pyroxene reflectance spectra: Minor absorption bands and effects of elemental substitutions. *Journal of Geophysical Research* 107, doi:10.1029/2001JE001590.

Cloutis E. A. and Gaffey M. J. 1991a. Pyroxene spectroscopy revisited—Spectral-compositional correlations and relationship to geothermometry. *Journal of Geophysical Research* 96: 22,809–22,826.

Cloutis E. A. and Gaffey M. J. 1991b. Spectral-compositional variations in the constituent minerals of mafic and ultramafic assemblages and remote-sensing implications. *Earth, Moon, and Planets* 53:11–53.

Cochran A. L. and Vilas F. 1998. The changing spectrum of Vesta: Rotationally resolved spectroscopy of pyroxene on the surface. *Icarus* 134:207–212.

Dowty E. and Lindsley D. H. 1973. Mössbauer spectra of synthetic hedenbergite-ferrosilite pyroxenes. *American Mineralogist* 58: 850–868.

Dyar M. D., Agresti D. G., Schaefer M. W., Grant C. A., and Sklute E. C. 2006. Mössbauer spectroscopy of earth and planetary materials. *Annual Review of Earth and Planetary Sciences* 34: 83–125.

Dyar M. D., Klima R. K., Lindsley D. H., and Pieters C. M. 2007. Effects of differential recoil-free fraction on ordering and site occupancies in Mössbauer spectroscopy of orthopyroxenes. *American Mineralogist* 92:424–428.

Evans B. J., Ghose S., and Hafner S. 1967. Hyperfine splitting of Fe^{57} and Mg-Fe order-disorder in orthopyroxenes ($MgSiO_3$-$FeSiO_3$ solid solution). *Journal of Geology* 75:306–322.

Gaffey M. J., Burbine T. H., and Binzel R. P. 1993. Asteroid spectroscopy—Progress and perspectives. *Meteoritics* 28:161–187.

Ghose S. 1965. Mg^{2+}-Fe^{2+} order in an orthopyroxene, $Mg_{0.93}Fe_{1.07}Si_2O_6$. *Zeitschrift für Kristallographie* 122:81–99.

Ghose S. and Wan C. 1973. Luna 20 pyroxenes: Evidence for a complex thermal history. Proceedings, 4th Lunar Science Conference. pp. 901–907.

Ghose S., Wan C., and McCallum I. S. 1975. Late thermal history of lunar anorthosite 67075: Evidence from cation order in olivine and orthopyroxene (abstract). 6th Lunar Science Conference. pp. 282–283.

Goldman D. S. and Rossman G. R. 1979. Determination of quantitative cation distribution in orthopyroxenes from electronic absorption spectra. *Physics and Chemistry of Minerals* 4:43–53.

Golubeva L. F. and Shestopalov D. I. 1997. Spectrometry of 4 Vesta near 505 nm pyroxene absorption band (abstract #1685). 28th Lunar and Planetary Science Conference. CD-ROM.

Golubeva L. F. and Shestopalov D. I. 2006. Are there pyroxenes on A-asteroid surfaces? (abstract #1228). 37th Lunar and Planetary Science Conference. CD-ROM.

Hamilton V. E. 2000. Thermal infrared emission spectroscopy of the pyroxene mineral series. *Journal of Geophysical Research* 105: 9701–9716.

Hazen R. M., Bell P. M., and Mao H. K. 1978. Effects of compositional variation on absorption spectra of lunar pyroxenes. Proceedings, 9th Lunar and Planetary Science Conference. pp. 2919–2934.

Molin G. M., Saxena S. K., and Brizi E. 1991. Iron-magnesium order-disorder in an orthopyroxene crystal from the Johnstown meteorite. *Earth and Planetary Science Letters* 105:260–265.

Mustard J. F., Poulet F., Gendrin A., Bibring J. P., Langevin Y., Gondet B., Mangold N., Bellucci G., and Altieri F. 2005. Olivine and pyroxene, diversity in the crust of Mars. *Science* 307:1594–1597.

Nash D. B. and Conel J. E. 1974. Spectral reflectance systematics for mixtures of powdered hypersthene, labradorite, and ilmenite. *Journal of Geophysical Research* 79:1615–1621.

Pieters C. M. 1993. Compositional diversity and stratigraphy of the Lunar crust derived from reflectance spectroscopy. In *Remote geochemical analysis: Elemental and mineralogical composition,* edited by Pieters C. M. and Englert P. A. J. Cambridge: Cambridge University Press. pp. 309–339.

Pieters C. M. and McFadden L. A. 1994. Meteorite and asteroid reflectance spectroscopy: Clues to early solar system processes. *Annual Review of Earth and Planetary Sciences* 22: 457–497.

Pollack S. S. 1968. Disordered pyroxene in chondrites. *Geochimica et Cosmochimica Acta* 32:1209–1217.

Preston R. S., Hanna S. S., and Heberle J. 1962. Mössbauer effect in metallic iron. *Physical Review A* 128:2207–2218.

Saxena S. K. and Ghose S. 1971. Mg^{2+}-Fe^{2+} order-disorder and the thermodynamics of the orthopyroxene crystalline solution. *American Mineralogist* 56:532–559.

Sunshine J. M. and Pieters C. M. 1993. Estimating modal abundances from the spectra of natural and laboratory pyroxene mixtures using the modified Gaussian model. *Journal of Geophysical Research* 98:9075–9087.

Sunshine J. M., Pieters C. M., and Pratt S. F. 1990. Deconvolution of mineral absorption bands—An improved approach. *Journal of Geophysical Research* 95:6955–6966.

Sunshine J. M., Pieters C. M., Pratt S., and McNaron-Brown K. S. 1999. Absorption band modeling in reflectance spectra: Availability of the modified Gaussian model (abstract #1306). 30th Lunar and Planetary Science Conference. CD-ROM.

Turnock A. C., Lindsley D. H., and Grover J. E. 1973. Synthesis and unit cell parameters of Ca-Mg-Fe pyroxenes. *American Mineralogist* 58:50–59.

Van Alboom A., De Grave E., and Vandenberghe R. E. 1993. Study of the temperature dependence of the hyperfine splitting parameters in two orthopyroxenes by ^{57}Fe Mössbauer spectroscopy. *Physics and Chemistry of Minerals* 20:263–275.

Vilas F., Cochran A. L., and Jarvis K. S. 2000. Vesta and the vestoids: A new rock group? *Icarus* 147:119–128.

Virgo D. 1973. Clinopyroxenes from Apollo 15: Fe^{2+}, Mg intracrystalline distributions (abstract). 4th Lunar Science Conference. pp. 749–751.

Virgo D. and Hafner S. S. 1970. Fe^{2+}, Mg order-disorder in natural orthopyroxenes. *American Mineralogist* 55:201–223.

Wivel C. and Mørup S. 1981. Improved computational procedure for evaluation of overlapping hyperfine parameter distributions in Mössbauer spectra. *Journal of Physics E: Scientific Instruments* 14:605–610.